

# Low-light Image Enhancement via the Absorption-Light-Scattering-Model

First A. Yun-fei Wang, Second B. He-ming Liu, and Third C. Zhao-wang Fu

**Abstract**—Low light often leads to poor image visibility, which can easily affect the performance of computer vision algorithms. First, this paper proposes the absorption light scattering model (ALSM), which can be used to reasonably explain the absorbed light imaging process for low-light images. In addition, the absorbing light scattering image obtained via ALSM under sufficient and uniform illumination can reproduce hidden outlines and details from the low-light image. Then, we identify that the minimum channel of absorption light scattering image obtained above exhibits high local similarity. This similarity can be constrained by superpixels, which effectively prevent the use of gradient operations at the edges so that the noise is not amplified quickly during enhancement. Finally, by analyzing the monotonicity between the scene reflection and the atmospheric light or transmittance in ALSM, a new low-light image enhancement method is identified. We replace atmospheric light with inverted atmospheric light to reduce the contribution of atmospheric light in the imaging results. Moreover, a soft jointed mean-standard-deviation (MSD) mechanism is proposed that directly acts on the patches represented by the superpixels. The MSD can obtain a smaller transmittance than that obtained by the minimum strategy, and it can be automatically adjusted according to the information of the image. Experiments on challenging low-light images are conducted to reveal the advantages of our method compared with other powerful techniques.

**Index Terms**—Low-light image enhancement, Absorption-light-scattering-model, Mean-standard-deviation, Minimal channel.

## I. INTRODUCTION

The vast majority of information acquired by humans comes from vision, and images are the main carrier of visual information [1]. Therefore, obtaining useful information from images has remained an important task of computer vision. However, under the impact of low light, image details are masked, resulting in a serious decline in image quality and problems such as low contrast, low visibility, and noise. These problems severely degrade the performance of many computer vision algorithms that require high-quality inputs (object detection, tracking, etc.) [1], [2]. To ensure that the information covered in these images is clearly visible, it is necessary to study low-light enhancement methods. For imaging reasons, low-light images captured by camera sensors are produced without sufficient illumination. To address this problem, the

Manuscript received 2018; revised ,2019; accepted 2019; Date of publication 2019; date of current version, 2019. This work was supported in part by the National Natural Science Foundation of China under grant 6150345.

The authors are with Laboratory of Information Processing, the school of Air Force Engineering University, Xian, 710051, China

(e-mail: wyfpost@163.com; liuheming1984@163.com; fuzw@126.com)

Color versions of one or more of the figures in this paper are available online at <http://ieeexplore.ieee.org>.

Digital Object Identifier

brightness and contrast of the degraded image must be improved [3].

In recent years, with the rapid development of convolutional neural network technology [4]-[12], deep learning methods relying on multiple image samples have made great progress. Although these methods have achieved remarkable results in the field of low-light enhancement, the disadvantages are also obvious. Learning-based methods rely on complex network structures and a large number of samples; thus, their training processes consume extensive hardware resources (GPU, RAM, etc.), and the training time cannot be tolerated. Moreover, the acquisition of the sample itself is not easy, as it is difficult to collect real image data under both low-light and normal illumination conditions. Therefore, many training data are synthesized by applying gamma correction to natural image patches, which may lead to unnatural results. To overcome these problems, scholars are constantly improving and optimizing their methods, and have made good progress. For example, using the See-in-the-Dark dataset, Chen developed a pipeline for processing low-light images with low photon counts and low signal-to-noise ratios (SNRs) based on the end-to-end training of a fully convolutional network [9]. Lore proposed a low-light net using deep autoencoders to perform contrast enhancement [10]. Inspired by gamma-band oscillations and other neurobiological discoveries, K. Zhan presented a feature-linking model (FLM) that uses the timing of spikes to encode information, which can boost the details of the input image while preserving the information [11]. K. Zhan also proposed a linking synaptic computation network (LSCN) for image enhancement that executes quickly and achieves a significant effect [12].

Due to the ease of image sample acquisition and reduced hardware requirements, the low-light enhancement of single images has remained a hotspot in this field of research. However, we cannot ignore the limitations of information in single images. Therefore, it is necessary to use a reasonable physical model to describe the imaging process for low-light images. An important and effective solution for this issue is image enhancement based on Retinex theory. The theory decomposes an image into reflectance and illumination. The early methods based on this theory aimed to improve reflectance, but these methods were prone to over-enhancement [13], [14]. To overcome this problem, Fu improved the contrast by adjusting illumination; however, rich texture information was easily lost due to the lack of illumination structure [15]. Wang proposed a bright-pass filter that acted on reflectance and illumination while trying to retain the details and naturalness of

the image [16]. Fu proposed a weighted variational model that could enhance the target image by simultaneously estimating reflectance and illumination [17]. However, both of these methods were not ideal for balancing reflectance and illumination, which affected the final imaging result [16], [17]. The method proposed by Guo [18] refined the initial illumination map by imposing a structure-aware prior. In most Retinex-based algorithm, logarithmic transformation is adopted to simplify the model. However, the noise that exists in low-light images is also amplified during this process. Considering the inherent defects of the logarithmic mechanism when applied to the Retinex model, Fu found that a linear domain model could better represent prior information to more accurately estimate reflectance and illumination than the logarithmic domain; however, the illumination of most natural low-light images was not uniformly distributed, which indicates that using  $\ell_2$  norm to enforce a spatially smooth illumination is not appropriate [19]. In addition, Li presented a robust Retinex model (RRM) by adding a noise term to handle low-light image enhancement under intense noise. Although RRM showed excellent noise suppression ability, it had difficulty balancing piecewise smoothed illumination and the structure of the revealed reflectance [20].

Researchers have attempted to enhance low-light images in other ways. The typical practice is to treat an inverted low-light image as a foggy image [21]; thus, many defogging methods can be applied to correct this issue [22]-[35], and the result of defogging is inverted once more to produce the enhanced result. However, this method lacks the necessary physical model to support the imaging process of low-light images. In this paper, we did not follow the classical Retinex-based illumination decomposition theory or the convolutional neural network learning approach [4]-[12]. Instead, we propose a new theoretical model called the absorption light scattering model (ALSM), which attempts to improve the quality of low-light images using atmospheric light and transmittance. In summary, there are four main contributions of this paper, as follows:

- We carefully analyzed and studied the atmospheric scattering model (ASM). Based on this model, we obtained the ALSM through mathematical deformation, which can reasonably explain the absorbed light imaging process for low-light images. ALSM makes the outlines and details that are masked in the low-light image appear under sufficient and uniform illumination, which is convenient for extracting features.
- We found that the minimum of each color channel in the absorption light scattering image obtained under sufficient and uniform illumination was the result of the joint influence of medium scattering, depth of field, and material reflective properties. From a numerical point of view, these features exhibit a high local similarity. This similarity can be constrained by superpixels, which effectively avoids gradient operations at the edges so that noise is not amplified quickly during enhancement.
- We found that enhancing the reflection of the scene can indirectly enhance low-light images. By analyzing the monotonicity between scene reflection and atmospheric

light or transmittance, a new method of low-light image enhancement is created. We replaced atmospheric light with inverted atmospheric light to reduce the contribution of atmospheric light to imaging results, and a soft jointed mean-standard-deviation (MSD) mechanism is proposed that directly acts on the patches represented by superpixels. Compared with the minimum strategy, MSD can obtain a smaller transmittance and can be automatically adjusted according to the information of the image.

- In comparison, we propose the locally restricted standard deviation (LRSD) assessment metric. This metric uses the standard deviation to measure the damage from noise to the local feature similarity, which is constrained by superpixels during enhancing,

## II. LOW-LIGHT IMAGE ENHANCEMENT

### A. Absorption Light Scattering Model

Based on the attenuation and ambient light model proposed by McCartney, Narasimhan and Nayar proposed a monochromatic ASM [36], [37], which reasonably explains the effects of particle scattering on visible light imaging. Atmospheric light is rarely the sole illumination source, as sunlight may go through the atmosphere and illuminate the objects [29],[30]. Under the premise that the light distribution is spatially constant, the form of ASM is given as follows:

$$\mathbf{I}(\mathbf{x}) = (\mathbf{SL} + \mathbf{A})\mathbf{R}(\mathbf{x})t(\mathbf{x}) + \mathbf{A}(1-t(\mathbf{x})) \quad (1)$$

where  $\mathbf{I}$  and  $\mathbf{R}$  represent the 3D matrix of the observed image and the reflection of the scene, respectively,  $\mathbf{x}$  is a 2D vector representing the coordinates  $(x, y)$  of a pixel's position,  $\mathbf{I}(\mathbf{x})$  is a 3D RGB vector at a pixel  $\mathbf{x}$ ,  $\mathbf{I}_c$  is the 2D matrix of the color channel  $c$ ,  $I_c(\mathbf{x})$  is a scalar of the color channel  $c$  at a pixel  $\mathbf{x}$ ,  $\mathbf{R}(\mathbf{x})$  is a 3D vector at a pixel  $\mathbf{x}$ ,  $R_c(\mathbf{x})$  is a scalar of the color channel  $c$  at a pixel  $\mathbf{x}$ ,  $t(\mathbf{x})$  is the medium transmittance of each point  $\mathbf{x}$ , and it is a scalar in  $[0, 1]$ , and  $\mathbf{SL}$  and  $\mathbf{A}$  represent the sunlight and the global atmospheric light of the scene, respectively.  $\mathbf{A}$  and  $\mathbf{SL}$  are 3D matrices usually assumed to be spatially constant; that is, they are constant matrices for each color channel  $c$  in  $\mathbf{I}$ .

However, for low-light scenes, insufficient illumination and uneven distribution are the main problems, and obtaining valuable features from low-light scenes is difficult. Therefore, the atmospheric light  $\mathbf{A}$  is nonconstant in this situation [29],[30], it is a variable  $\mathbf{A}(\mathbf{x})$  related to position  $\mathbf{x}$ , and  $\mathbf{A}(\mathbf{x})$  is a 3D vector at a pixel  $\mathbf{x}$ ,  $\mathbf{A}_c$  is the 2D matrix of the color channel  $c$ ,  $A_c(\mathbf{x})$  is a scalar of the color channel  $c$  at a pixel  $\mathbf{x}$ . In addition, point light sources (natural or artificial) may exist in special cases (see Fig.1). Unfortunately, these point light sources have very limited illumination ranges and cannot light surrounding objects such as the sunlight in (1); thus, they can be regarded as part of the global atmospheric light, and we can ignore sunlight and modify (1) as follows:

$$\mathbf{I}(\mathbf{x}) = \mathbf{A}(\mathbf{x})\mathbf{R}(\mathbf{x})t(\mathbf{x}) + \mathbf{A}(\mathbf{x})(1-t(\mathbf{x})) \quad (2)$$

The first term on the right-hand side, i.e.,  $\mathbf{A}(\mathbf{x})\mathbf{R}(\mathbf{x})t(\mathbf{x})$ , is called direct-attenuation, and the second term, i.e.,

$\mathbf{A}(\mathbf{x})(1-t(\mathbf{x}))$ , is called air-light [30]. Because  $\mathbf{A}(\mathbf{x})$  has a great impact on both direct-attenuation and air-light, if  $\mathbf{A}(\mathbf{x})$  is very small, then dim imaging results can be obtained. Although the above can explain the reasons for low-light imaging to a certain extent, obtaining useful information from dim scenes is difficult. Obviously, ASM is not suitable for low-light enhancement problems.



Fig.1 Point light sources in low-light images

Thus,  $\mathbf{A}(\mathbf{x})\mathbf{R}(\mathbf{x})$  in equation (2) represents the scene radiance, which describes the portion of atmospheric light that is reflected from the scene. It is natural to think of  $\mathbf{A}(\mathbf{x})(1-\mathbf{R}(\mathbf{x}))$  as the scene absorption, which describes the portion of the atmospheric light that is absorbed by the scene. According to this analysis, we transform equation (2):

$$\mathbf{A}(\mathbf{x}) \cdot \mathbf{I}(\mathbf{x}) = \mathbf{A}(\mathbf{x})(1 - \mathbf{R}(\mathbf{x})) \cdot t(\mathbf{x}) \quad (3)$$

This modification, which is referred to as the ALSM in this paper, is a new physical model that can be used as a basis for the formation of low-light images. The physical meaning of this model is that the scene itself is considered illuminant. In the absence of external light, all absorbed light is radiated, and the light directly reaches the camera without scattering, forming the absorption light scattering image on the left-hand side of equation (3). To simplify the expression of ALSM, we can transform equation (3):

$$1 - \frac{\mathbf{I}(\mathbf{x})}{\mathbf{A}(\mathbf{x})} = (1 - \mathbf{R}(\mathbf{x})) \cdot t(\mathbf{x}) \quad (4)$$

### B. Monotonic Analysis

For the implicit ALSM function represented in (4), the number of pixels in an image is denoted by  $N$ . If  $\mathbf{I}(\mathbf{x})$  is an RGB color image, then the scalars  $I_c(\mathbf{x})$ ,  $R_c(\mathbf{x})$  and  $A_c(\mathbf{x})$  are the components in the channel  $c \in \{R, G, B\}$ . However, we have  $3N$  unknown reflections  $R_c(\mathbf{x})$ ,  $3N$  unknown global atmospheric light  $A_c(\mathbf{x})$  and  $N$  unknown transmission  $t(\mathbf{x})$ . The total number of unknowns are  $7N$ , which is much greater than the number  $3N$  of knowns  $I_c(\mathbf{x})$ . Thus, this problem is ill-posed and requires extra constraints to solve [30]. Thus, we need to analyze the monotonicity between variables by means of isolation. If we consider each color channel  $c$  at each pixel  $\mathbf{x}$  in  $\mathbf{I}$  and regard  $I_c(\mathbf{x})$  as a sole function of  $R_c(\mathbf{x})$ , then we can obtain:

$$\frac{dI_c(\mathbf{x})}{dR_c(\mathbf{x})} = A_c(\mathbf{x})R_c(\mathbf{x}) \quad A_c(\mathbf{x}) \geq 0, 0 \leq R_c(\mathbf{x}) \leq 1 \quad (5)$$

The expression (5) indicates that, at any pixel  $\mathbf{x}$  in  $\mathbf{I}$  with a fixed color channel  $c$ ,  $I_c(\mathbf{x})$  increases monotonically with increased  $R_c(\mathbf{x})$ . Thus, the low-light enhancement problem becomes a scene reflection  $\mathbf{R}(\mathbf{x})$  improvement problem.

In (4), the factors affecting  $\mathbf{R}(\mathbf{x})$  are  $\mathbf{A}(\mathbf{x})$  and  $t(\mathbf{x})$ . To

avoid confusion of concepts and for convenience of calculating the derivative, we replace  $\mathbf{A}(\mathbf{x})$  with  $a(\mathbf{x})$ . If we consider each color channel  $c$  at each pixel  $\mathbf{x}$  in  $\mathbf{I}$ , then we can obtain:

$$1 - \frac{I_c(\mathbf{x})}{a_c(\mathbf{x})} = (1 - R_c(\mathbf{x})) \cdot t(\mathbf{x}) \quad a_c(\mathbf{x}) \geq 0, 0 \leq t(\mathbf{x}) \leq 1 \quad (6)$$

In (6), we first regard  $R_c(\mathbf{x})$  as a function of  $a_c(\mathbf{x})$  and  $t(\mathbf{x})$ , denoted by  $R_c(\mathbf{x}) = f(a_c(\mathbf{x}), t(\mathbf{x})) = 1 - (1 - I_c(\mathbf{x})/a_c(\mathbf{x}))/t(\mathbf{x})$ . Then, we calculate the partial derivatives separately, and the outcome is

$$\frac{\partial R_c(\mathbf{x})}{\partial a_c(\mathbf{x})} = -\frac{I_c(\mathbf{x})}{\max(t(\mathbf{x}), \varepsilon)} \cdot \frac{1}{a_c(\mathbf{x})^2} \quad (7)$$

$$\frac{\partial R_c(\mathbf{x})}{\partial t(\mathbf{x})} = \frac{I_c(\mathbf{x}) - a_c(\mathbf{x})}{a_c(\mathbf{x})} \cdot \frac{1}{(\max(t(\mathbf{x}), \varepsilon))^2} \quad (8)$$

In (7) and (8),  $\varepsilon$  denotes an infinitesimal value that prevents this term from being indivisible. Expression (7) indicates that at any pixel  $\mathbf{x}$  in  $I_c(\mathbf{x})$  with a fixed color channel  $c$ ,  $R_c(\mathbf{x})$  increases monotonically with decreased  $a_c(\mathbf{x})$ . In the database of low-light images from a previous study [16], we calculate the maximum  $A_c$  at each pixel  $\mathbf{x}$  of  $A_c$ , and the average of the three channels is denoted by  $A$ . As shown in Fig.2, all images satisfy  $A > 0.5$ , which indicates  $0 < 1 - A < A$ . Thus, we can enhance  $R_c(\mathbf{x})$  in ALSM by replacing  $a_c(\mathbf{x})$  with  $1 - A_c$  at each point.

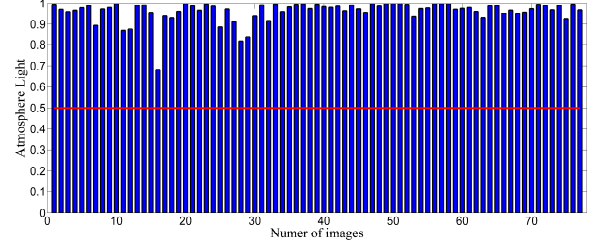


Fig.2 Atmosphere light in low-light images

On this basis, we focus on only the value of the molecule in equation (8). After calculation, Fig.3 shows that most pixels in low-light images satisfy the condition  $1 - A_c < I_c(\mathbf{x})$ . This result implies that  $R_c(\mathbf{x})$  increases monotonically with decreased  $t(\mathbf{x})$ .

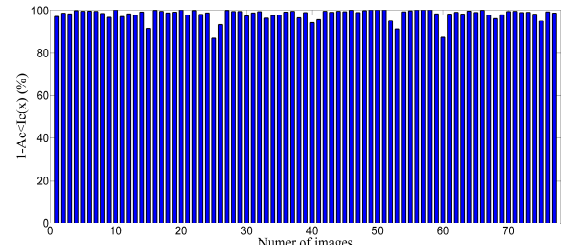


Fig.3. Percentage of pixels that satisfy  $1 - A_c < I_c(\mathbf{x})$  in low-light images

### C. Minimum Channel Constraint

ALSM not only physically finds the imaging mechanism of the absorption light scattering image, but it also reproduces the hidden details of low-light images and obtains additional features for analysis. We can obtain the brightest pixel value  $A_c$  for each color channel  $c$  in a low-light image  $\mathbf{I}$ . If we evenly illuminate each color channel of a low light scene with virtual external light  $A_c$ , and the low-light scene emits all the light that

is absorbed, the overall brightness of the scene will inevitably greatly increase, revealing many details. Thus, we consider each color channel  $c$  of each pixel  $\mathbf{x}$  in  $\mathbf{I}$ ; then, we can simplify equation (6):

$$1 - \frac{I_c(\mathbf{x})}{A_c} = (1 - R_c(\mathbf{x})) \cdot t(\mathbf{x}) \quad A_c = \max_{A_c(\mathbf{x}) \in A_c} \{A_c(\mathbf{x})\} \quad (9)$$

where  $I_c(\mathbf{x}) / A_c$  can be considered the normalization process of  $\mathbf{I}$ . All absorbed light is radiated, and the light directly reaches the camera without scattering, forming the absorption light scattering image under sufficient and uniform illumination  $A_c$  on the left-hand side of equation (9). Moreover, the absorption light scattering image must be numerically equivalent to create the complement of the normalized low-light image.

In (9), the scene can be divided into many independent objects. The atmosphere in which these objects are located is a homogeneous medium, which means that the medium scattering coefficient  $\beta$  remains constant. Points in these objects that are equidistant from the camera converge to form several very small regions, which ensures that  $d(\mathbf{x})$  remains constant. These two factors work together to keep  $t(\mathbf{x}) = \exp[-\beta d(\mathbf{x})]$  locally invariant [30]. However, points in local regions that make up the same object have similar physical properties, i.e.,  $I - R_c(\mathbf{x})$  is also invariant. Therefore, we can deduce that there is a high similarity in pixel values on the left-hand side of equation (9) in these small regions.

Because the human eye is not sensitive to changes in



(a) Normal lighting image

(b) Foggy image

(c) Absorbing light scattering image with  $A$ 

Fig.4 Minimal channels of different types of images

Mathematically, to further verify the validity of the minimum channel for describing local similarity, in the database [16], we use the TP algorithm [38] to segment the constructed 2D grayscale image  $\mathbf{S}$  with different strategies (min channel, middle channel, max channel), then calculate the mean value in each superpixel, and finally measure the interclass discrimination degree of different strategies by comparing the standard deviations between superpixels. The larger the value is, the higher the discrimination ability. From the results of Fig.5, the average standard deviation values of the strategies are 0.2377, 0.2139 and 0.1946, respectively. The minimum strategy has the highest value, which is consistent with previous observations. Furthermore, the ratio of the min channel strategy

grayscale, according to our observations, this similarity is reflected in the minimum value of each color channel  $c$  in the absorption light scattering image under sufficient and uniform illumination  $A_c$ , which can be seen as the result of the joint action of  $I - R_c(\mathbf{x})$ ,  $\beta$  and  $d(\mathbf{x})$ . (observed in Fig.4). Thus, because superpixels can aggregate similarly characterized pixels into very small and visually meaningful regions [38]-[42] and adhere the edges and textures of the image well, to constrain this local similarity, we directly apply the superpixel segmentation technique to  $\mathbf{S}$ , which is represented by

$$\mathbf{S} = \min_c \left( 1 - \frac{\mathbf{I}_c}{A_c} \right) \quad A_c = \max_{A_c(\mathbf{x}) \in A_c} \{A_c(\mathbf{x})\} \quad (10)$$

In (10), The right-hand side of the equation is the minimum of each fixed pixel  $\mathbf{x}$  for color channel  $c$ . This process has a natural advantage in terms of noise suppression. We know that dark areas of low-light images  $I$  are inevitably accompanied by noise. Let  $N$  denote the noise term; then,  $I = I' + N$ , where  $I'$  represents the pure image signal. Because noise and image details are high-frequency information and the noise itself is numerically one order of magnitude higher than the gradient operator, noise is particularly sensitive on edges or textures. However, in the area constrained by superpixels,  $I$  is isotropic and  $\nabla I$  is small, resulting in little change in  $\nabla I'$  and  $\nabla N$ . This condition effectively prevents the noise on the details from being amplified too quickly, which plays a role in noise suppression.

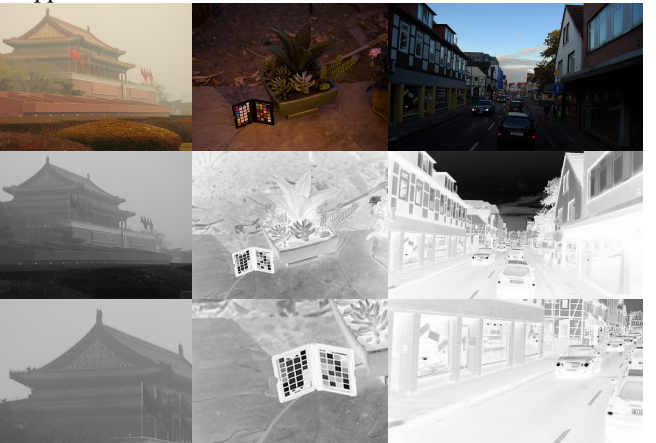
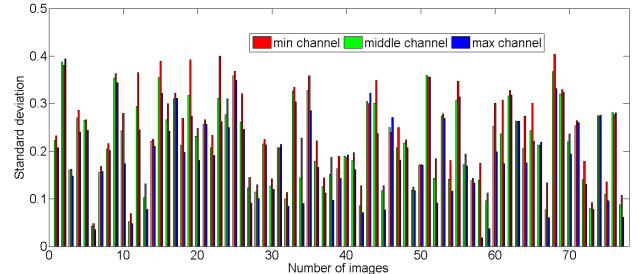


Fig.5 Inner-class standard deviation of superpixel

to the other two strategies reached 87.013%, but the failure of a small number of low-light images requires further study to determine its cause.



#### D. Mean standard deviation mechanism

Assuming that the  $i$ th superpixel is represented by  $\Omega_i$  and  $\Omega \subset S$ . In this paper, a novel MSD mechanism is proposed that directly acts on the  $\Omega_i$  and is presented as

$$MSD = \frac{1}{n} \sum_{j=1}^n x_j + k \sqrt{\frac{1}{n} \sum_{j=1}^n \left( x_j - \frac{1}{n} \sum_{j=1}^n x_j \right)^2} \quad (11)$$

where  $n$  is the number of pixels contained in  $\Omega_i$ , and  $k \in [-1, 1]$  is an enhanced effect regulator. On the right-hand side of equation (11), the first and second terms are the mean and standard deviation of all pixels in  $\Omega_i$ , respectively. According to the monotonic analysis in section B. to improve  $R_c(x)$ , the new form of the ALSM is given by

$$1 - \frac{I_c(x)}{(1 - A_c)} = (1 - R_c(x)) \cdot t(x) \quad A_c > 0, 0 \leq t(x) \leq 1 \quad (12)$$

Using the minimal channel as a priori knowledge and combined with the superpixel constraint and the MSD mechanism, acting on both sides of equation (12):

$$1 - MSD \left( \min_{x \in \Omega} \frac{I_c(x)}{1 - A_c} \right) = \left( 1 - MSD \left( \min_c R_c(x) \right) \right) \cdot \tilde{t}(x) \quad (13)$$

Assuming that the enhanced  $R_c(x) > 0$  is established in most cases, then  $0 < MSD \left( \min_c R_c(x) \right) < 1$  is established. To further reduce the value of  $\tilde{t}(x)$ , equation (13) can be simplified to

$$\tilde{t}(x) = 1 - MSD \left( \min_c \frac{I_c(x)}{1 - A_c} \right) \leq 1 - \min_{x \in \Omega} \left( \min_c \frac{I_c(x)}{1 - A_c} \right) \quad (14)$$

According to (11) and (14), the following can be analyzed: for darker points, transmittance should be reduced as much as possible to improve the enhancement, and a large MSD value is required; for brighter points, transmittance should be increased as much as possible to reduce enhancement, and a small MSD value is required. For the MSD to adaptively vary with the pixel value information, the value is constrained to  $[-1, 1]$ . When used for enhancement, the parameter  $k$  in (11) is given by:

$$k = \cos \left( \pi \cdot \frac{1}{n} \sum_{j=1}^n x_j \right) \quad 0 \leq \frac{1}{n} \sum_{j=1}^n x_j \leq 1 \quad (15)$$

Putting (15) into (11), a complete expression of MSD can be obtained:

$$MSD = \frac{1}{n} \sum_{j=1}^n x_j + \cos \left( \pi \cdot \frac{1}{n} \sum_{j=1}^n x_j \right) \cdot \sqrt{\frac{1}{n} \sum_{j=1}^n \left( x_j - \frac{1}{n} \sum_{j=1}^n x_j \right)^2} \quad (16)$$

The MSD mechanism can obtain a smaller transmittance than the minimum strategy, and it can be automatically adjusted according to the information of the image. To avoid the supersaturation problem during enhancement and make the enhancement effect controllable, this paper introduces the golden ratio and corrects equation (14) to

$$\tilde{t}(x) = 1 - \exp(-0.618^T) MSD \left( \min_c \frac{I_c(x)}{1 - A_c} \right) \quad T = 1, 2, 3, \dots \quad (17)$$

Once the atmospheric light and transmittance are estimated, we can obtain the scene reflection according to (12) and restrict the transmittance by a lower bound  $t_0$  to present this term from being indivisible. In our paper, a typical fixed value of  $t_0$  is 0.1.

$$R_c(x) = 1 + \left( \frac{I_c(x)}{1 - A_c} - 1 \right) \cdot \frac{1}{\max(\tilde{t}(x), t_0)} \quad (18)$$

In summary, the final enhancement results at pixel  $x$  of the low-light image is the scene radiance, which is given by:

$$(1 - A_c) R_c(x) = \frac{I_c(x) - (1 - A_c)}{\max(\tilde{t}(x), t_0)} + (1 - A_c) \quad (19)$$

### III. EXPERIMENTAL RESULT AND ANALYSIS

In this section, we evaluate the performance of our proposed enhancement method, which is called the ALSM algorithm. First, we present the processing flow of our algorithm. Then, we qualitatively and quantitatively compare ALSM with several state-of-the-art methods in terms of enhancement effect. After that, we further evaluate the ability of different algorithms to suppress noise amplification. Finally, we discuss and analyze the computational complexity of our method. We test images of various scenes from the datasets provided by Wang et al. [16], Fu [15], [17], [19], high dynamic range (HDR) [48], and NASA [43] and images from the Internet. All experiments are conducted in MATLAB 2014a on a PC running Windows 10 OS with 8G RAM and 1.8GHZ.

#### A. Processing Flow

ALSM mainly contains two parameters,  $n$  and  $T$ , which represent the number of pixels contained in  $\Omega$  and the enhancement effect adjustment factor, respectively. To obtain superpixels with a regular shape and good edge fit, our paper uses the TP algorithm [38] to segment  $S$ , and only parameter  $n$  needs to be set. If not specifically stated, the parameters  $n$  and  $T$  are set as 225 and 6 in our experiment, respectively. For clarity, the ALSM procedure is summarized in Algorithm 1. We also depict the intermediate processing results of ALSM in Fig.6.

---

#### Algorithm 1: ALSM

**Input:** Low-light Input  $I(x)$ , number of pixels in superpixel  $n$ , enhancement effect adjustment factor  $T$

**Do the job**

1. Estimate  $A_c$  using dark-channel-prior [29]
2. Compute  $S$  via Eq. (10)
3. Use the TP algorithm [38] to segment  $S$  to obtain  $\Omega$
4. Compute MSD via Eq. (16)
5. Estimate  $\tilde{t}(x)$  via Eq. (17)
6. Refine  $\tilde{t}(x)$  using a guided filter [44]
7. Enhance  $R(x)$  via Eq. (18)
8. Compute the scene radiance of each pixel via Eq. (19)

**Output:** Final enhanced result

---

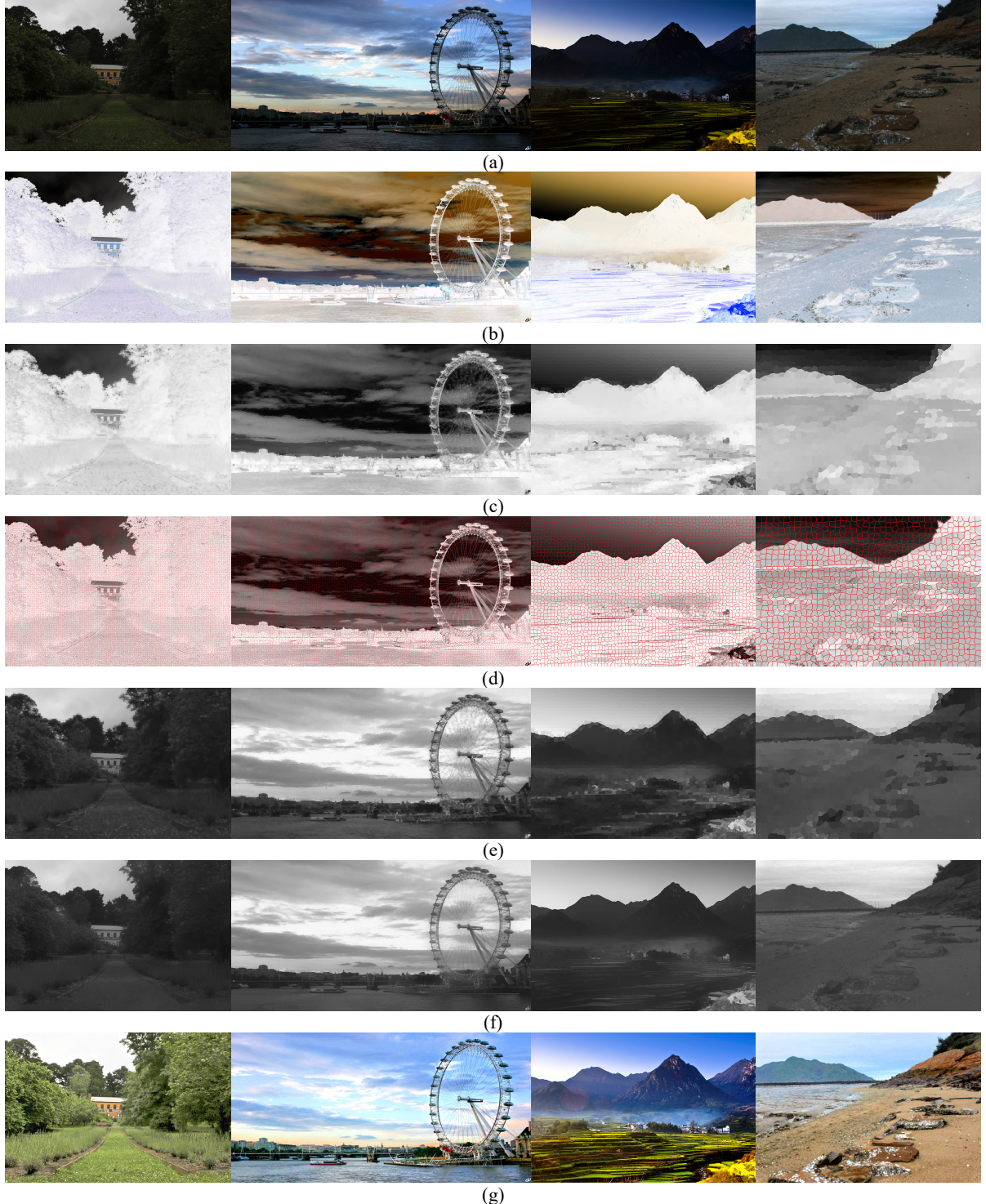


Fig.6. Intermediate decomposition results of ALSM. From top to bottom: (a) Input low-light image, (b) absorbing light scattering image with uniform illumination  $A$ , (c) minimal channel of absorbing light scattering image, (d) minimal channel constraint by superpixels, (e) rough transmittance, (f) refined transmittance, (g) ALSM result with  $T=6$ .

### B. Subjective comparisons

The method compared in this paper have better robustness, all results are generated via code downloaded from the authors' websites, and the original experimental parameter settings are used [11],[12],[15]-[20]. Several comparisons generated via different enhancement methods are displayed in Figs. 7, 8, 9,

and 11, including images with low illumination, backlighting and nonuniform illumination. In general, the enhancement results of LSCN [12], simultaneous reflectance and illumination estimation (SRIE) [17] and probabilistic image enhancement (PIE) [19] are dark, especially for backlight images, and the results do not show sufficient details (observed in Figs. 7, 8, 9, and 11).

Regarding local details, the FLM [11], SRIE [17], fusion-based enhancing (FBE) [15], and PIE [19] methods produced plaque problems, which can be observed in Fig.11. Although the naturalness preserved enhancement (NPE) method [16] can present rich details and textures, a serious color cast effect remains, which results in enhancement that is not sufficiently natural, and plaque phenomena also occur when processing the backlight image (observed in Fig. 9).

Similarly, the processing results of FLM [11] are brighter and can highlight many details. However, they also show serious color cast effect, which results in enhancement that is not sufficiently natural, producing an oil painting effect (observed in Figs. 7 and 8); plaque phenomena also occur when

processing the backlight image (observed in Fig.11). By comparison, the low-light illumination map estimation (LIME) method [18] illuminates dark regions and shows impressive performance in terms of texture and details. Nevertheless, this method sometimes overenhanced the regions with relatively high intensities, such as the local regions in Fig. 9. RRM [20] exhibited outstanding performance in terms of noise suppression, but smoothing constraint processing resulted in very blurry enhancement results, and many image details and textures were lost (observed in Figs. 7, 8, 9 and 11). In summary, the proposed ALSM method achieves a good balance between brightness, contrast, and texture details, and it can effectively enhance the visibility of low-light images.



Fig.7. Comparison of enhancement methods for the test image street. From (a) to (j): (a) Input low-light image, (b) feature-linking model for image enhancement (FLM) [11], (c) linking synaptic computation for image enhancement (LSCN) [12], (d) naturalness preserved enhancement (NPE) [16], (e) low-light illumination map estimation (LIME) [18], (f) probabilistic method for image enhancement (PIE) [19], (g) fusion-based enhancing method (FBE) method [15]. (h) simultaneous reflectance and illumination estimation (SRIE) [17], (i) robust Retinex model (RRM) [20], (j) ALSM with T=6.

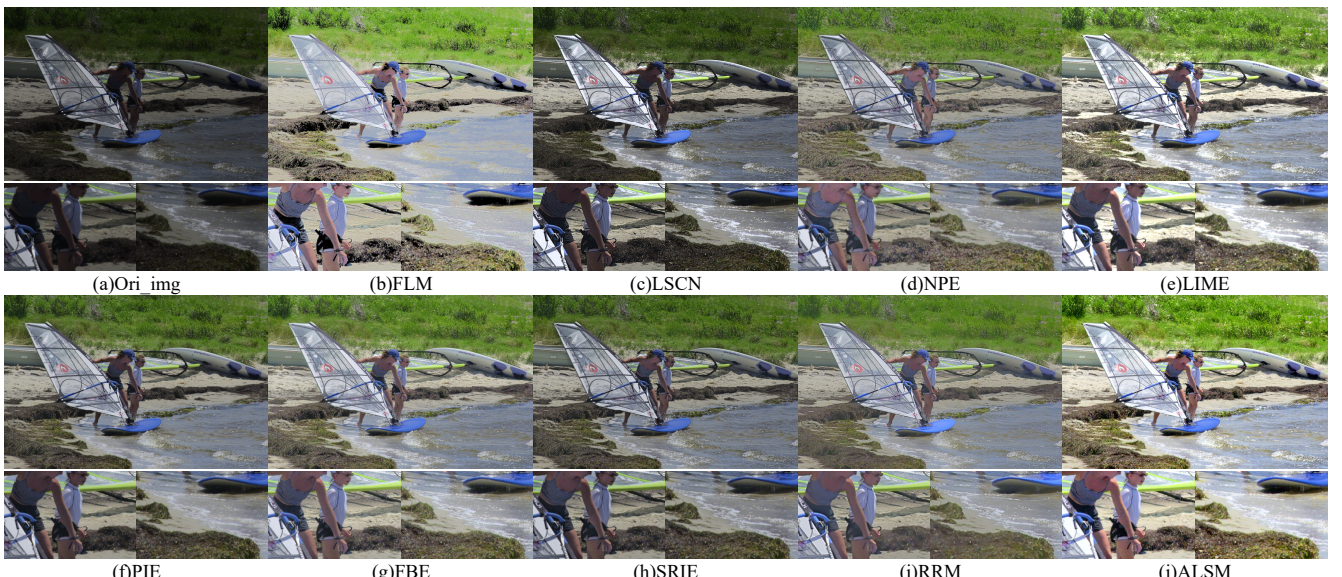


Fig.8. Comparison of enhancement methods for a surfing test image. From (a) to (j): (a) Input low-light image, (b) feature-linking model for image enhancement (FLM) [11], (c) linking synaptic computation for image enhancement (LSCN) [12], (d) naturalness preserved enhancement (NPE) [16], (e) low-light illumination map estimation (LIME) [18], (f) probabilistic method for image enhancement (PIE) [19], (g) fusion-based enhancing method (FBE) method [15]. (h) simultaneous reflectance and illumination estimation (SRIE) [17], (i) robust Retinex model (RRM) [20], (j) ALSM with T=6.



Fig.9. Comparison of enhancement methods for a test image of a woman. From (a) to (j): (a) Input low-light image, (b) feature-linking model for image enhancement (FLM) [11], (c) linking synaptic computation for image enhancement (LSCN) [12], (d) naturalness preserved enhancement (NPE) [16], (e) low-light illumination map estimation (LIME) [18], (f) probabilistic method for image enhancement (PIE) [19], (g) fusion-based enhancing method (FBE) method [15]. (h) simultaneous reflectance and illumination estimation (SRIE) [17], (i) robust Retinex model (RRM) [20], (j) ALSM with  $T=6$ .

### C. Objective quality assessments

Relying on only subjective visual comparison is not convincing; thus, objective evaluation indicators are also required. Because assessing the quality of enhanced images is not a unique task, there have been a large number of image quality assessment (IQA) indicators in recent years [46],[47]. We believe that the three most important aspects of IQA are brightness, contrast, and local details. Therefore, we adopt four blind IQAs in our assessment, i.e., brightness [2], global contrast factor (GCF) [45], no-reference free energy-based robust metric for contrast distortion (NIQMC) [46], and blind image quality measure of enhanced images (BIQME) [47].

a. According to the visual characteristics of the human eye, sufficient brightness is crucial for seeing objects. In this paper, we convert an image into the HSV space and obtain the mean value of the V component as the brightness. A higher brightness always indicates better image clarity.

b. The GCF [45] uses contrasts at various resolution levels to compute the overall contrast of an image. A higher GCF always indicates more noticeable details, which usually results in better image quality. Because this method is suitable for only grayscale processing, we map the RGB components to the grayscale space according to the weight relationship of the human eye, and then process it with GCF.

c. NIQMC [46], assesses image quality by measuring local details and creating a global histogram of the given image, and it particularly favors images with higher contrast. Thus, higher NIQMC values indicate better image contrast quality.

d. BIQME [47] comprehensively considers five influencing factors, i.e., contrast, sharpness, brightness, colorfulness, and naturalness, and 17 associated features to blindly predict visual quality. This assessment metric uses a regression module learned with big-data training samples. A higher BIQME indicates better image quality.

We use these four assessment indicators for a dataset containing 80 low-light images, consisting of images from the Wang [16], Fu [15], [17], [19] and NASA [43] datasets. For

each assessment metric, the average of the assessment results for 80 images enhanced by different methods is shown in Fig.10. The data in Fig.10 show that, in addition to brightness, the ALSM algorithm proposed in this paper has the highest score. Although FLM is very eye-catching in terms of brightness, it is not satisfactory on other indicators, and it loses some image information. Overall, the enhancement effect of ALSM is the best of all the algorithms.

### D. Noise suppression assessment

Low-light image enhancement is often accompanied by noise amplification, and noise is high-frequency information; the edges of the image and areas with abundant texture are sensitive to noise. Superpixels are composed of similar pixels that are clustered into visually meaningful microscopic regions that closely fit the edges or textures of the image. Therefore, the variation in the pixels in  $\Omega_i$  is small. Thus, we combine the standard deviation (SD) mechanism with superpixel technology and propose the LRSD assessment metric. This metric considers that a high-definition image is isotropic and uniform in  $\Omega_i$ , and thus the SD of the feature is relatively small in this local area; SD grows only under the effect of noise. Let  $M$  be the number of  $\Omega_i$  in the image; then, LRSD is given by

$$\left\{ \begin{array}{l} SD = \sqrt{\frac{1}{n} \sum_{j=1}^n \left( x_j - \frac{1}{n} \sum_{j=1}^n x_j \right)^2} \\ LRSD = \frac{1}{M} \sum_{i=1}^M SD \end{array} \right. \quad (20)$$

In (20), LRSD must first segment the reference image with superpixel technology [38] to obtain  $\Omega_i$ . Then, in each  $\Omega_i$  of the enhanced image, SD is used to measure the damage to the local feature similarity under the influence of noise. In our paper, local features are presented as color and expressed in the RGB color space. LRSD does not consider the impact of noise on structure and detail; thus, three other full-reference IQA assessment indicators are introduced to make up for this deficiency. Because few datasets with ground-truth images are

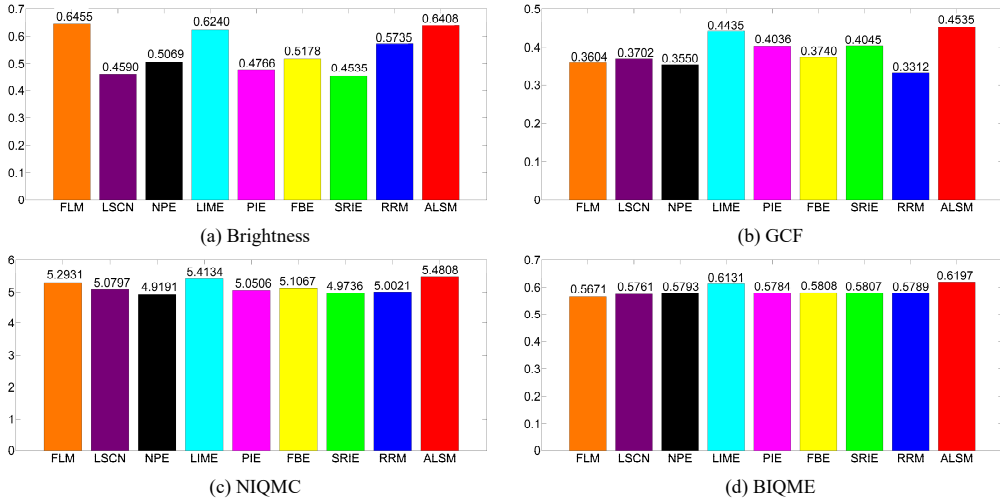


Fig.10. Comparison of the assessment indicators for the enhancement methods.

publicly available. We adopt the HDR [48] reconstruction results from a set of bracketed exposures as a ground-truth reference.

Table I shows the numerical comparison results of IW-PSNR [49] for all competitors on the HDR dataset [48]. From the average of the results, we can see that ALSM( $T=4$ ) has the second highest signal-to-noise ratio of all methods. Although FBE scores the highest, it is largely affected by pseudo-details or structural information (observed in Fig.10). In addition, as parameter  $T$  increases, the noise suppression ability of ALSM decreases with the improvement in the enhancement effect. This result reflects the inability of ALSM to cope with excessive noise density. In contrast, RRM has shown robust noise immunity [20].

Tables II and III show the numerical comparison results of the two improved indicators of the structural similarity index measure (SSIM) [49]. The average MS-SSIM or IW-SSIM of ALSM( $T=4$ ) ranks 2nd among the compared methods. Although LIME scores the highest, the numerical results in

Table IV exceed the scores for the reference image, indicating that the high score of the LIME method is largely affected by noise rather than real details or structural information.

Table IV shows the numerical comparison results of LRSD for all competitors on the HDR dataset. From the average of the results, we can see that ALSM( $T=4$ ) still ranks second among the compared methods. Although RRM [20] scores the lowest of all methods, the average numerical results in Table II and Table III rank last. This result shows that RRM enhancement results are very vague.

In general, the ALSM is accompanied by noise amplification during enhancement. This method not only achieved a good balance in terms of structure, detail and local feature similarity, but it also exhibited a certain ability to suppress low-density noise. Correspondingly, the results of the different methods for the “SantasLittleHelper” test image are shown in Fig. 11, and these results are consistent with the data reflected in the full reference objective indicators described above.

TABLE I  
Comparison of IW-PSNR for different methods

Images (1358 x 900)	Ori	Methods											
		FLM	LSCN	NPE	LIME	PIE	FBE	SRIE	RRM	ALSM( $T=4$ )	ALSM( $T=5$ )	ALSM( $T=6$ )	ALSM( $T=7$ )
BabyAtWindow	1000	18.47	18.55	21.06	22.11	21.68	22.31	22.37	18.37	20.93	20.23	19.61	19.14
BabyOnGrass	1000	18.99	18.76	20.49	23.08	21.81	22.21	22.03	18.10	23.52	23.18	22.69	22.26
ChristmasRider	1000	19.49	16.69	18.69	19.13	20.20	21.75	19.84	18.75	20.71	20.70	20.48	20.21
FeedingTime	1000	20.36	19.47	21.48	19.36	22.67	23.37	22.19	21.20	22.29	21.64	21.07	20.65
HighChair	1000	18.33	19.98	21.56	18.92	21.74	22.09	21.50	20.50	20.97	20.27	19.68	19.24
LadyEating	1000	15.47	15.04	16.21	14.69	16.22	16.64	16.17	16.08	15.82	15.64	15.45	15.24
PianoMan	1000	17.40	15.07	16.83	20.50	18.54	19.53	18.62	16.77	20.02	20.39	20.37	20.15
SantasLittleHelper	1000	21.05	17.59	20.76	20.49	21.49	23.25	21.11	20.21	21.76	21.49	20.90	20.28
Average	1000	18.70	17.64	19.64	19.79	20.54	<b>21.39</b>	20.48	18.62	20.75	20.44	20.03	19.64

TABLE II  
Comparison of MS-SSIM for different methods

Images (1358 x 900)	Ori	Methods											
		FLM	LSCN	NPE	LIME	PIE	FBE	SRIE	RRM	ALSM( $T=4$ )	ALSM( $T=5$ )	ALSM( $T=6$ )	ALSM( $T=7$ )
BabyAtWindow	1	0.8495	0.8361	0.8952	0.9503	0.9004	0.9179	0.8970	0.8393	0.9208	0.9170	0.9096	0.9015
BabyOnGrass	1	0.7785	0.8195	0.8442	0.9471	0.8978	0.9074	0.8971	0.7715	0.9314	0.9297	0.9256	0.9214
ChristmasRider	1	0.8054	0.6535	0.7333	0.8582	0.8117	0.8420	0.8074	0.7373	0.8503	0.8552	0.8531	0.8483
FeedingTime	1	0.8464	0.8759	0.9324	0.9086	0.9324	0.9344	0.9093	0.8845	0.9229	0.9134	0.9042	0.8965
HighChair	1	0.7829	0.8758	0.8719	0.8899	0.9240	0.9217	0.9039	0.8868	0.9114	0.8936	0.8775	0.8649
LadyEating	1	0.6417	0.6835	0.6647	0.7326	0.7555	0.7580	0.7347	0.7428	0.7607	0.7562	0.7449	0.7324
PianoMan	1	0.8188	0.6761	0.7557	0.9280	0.8378	0.8700	0.8326	0.7668	0.8846	0.8997	0.9050	0.9045
SantasLittleHelper	1	0.8532	0.7066	0.8136	0.9142	0.8731	0.8945	0.8621	0.7952	0.9077	0.9126	0.9085	0.9008
Average	1	0.7971	0.6564	0.8139	<b>0.8911</b>	0.8666	0.8807	0.8556	0.8030	0.8862	0.8847	0.8786	0.8713

TABLE III  
Comparison of IW-SSIM for different methods

Images (1358 x 900)	Ori	FLM	LSCN	NPE	LIME	PIE	FBE	Methods					
								SRIE	RRM	ALSM(T=4)	ALSM(T=5)	ALSM(T=6)	ALSM(T=7)
BabyAtWindow	1	0.8131	0.8208	0.8782	0.9309	0.8838	0.8951	0.8917	0.8095	0.8971	0.8912	0.8820	0.8727
BabyOnGrass	1	0.7474	0.8057	0.8325	0.9399	0.8861	0.9002	0.8925	0.7472	0.9240	0.9219	0.9174	0.9128
ChristmasRider	1	0.7997	0.6360	0.7385	0.8538	0.8129	0.8421	0.8140	0.7288	0.8545	0.8604	0.8582	0.8529
FeedingTime	1	0.8168	0.8515	0.8654	0.8871	0.9200	0.9226	0.9062	0.8619	0.9128	0.9026	0.8925	0.8840
HighChair	1	0.7408	0.8473	0.8545	0.8586	0.9017	0.8983	0.8882	0.8601	0.8846	0.8636	0.8448	0.8300
LadyEating	1	0.5090	0.5298	0.5369	0.5753	0.5957	0.6004	0.5860	0.6057	0.6109	0.6087	0.5987	0.5877
PianoMan	1	0.8045	0.6571	0.7522	0.9239	0.8260	0.8607	0.8290	0.7614	0.8805	0.8967	0.9021	0.9014
SantasLittleHelper	1	0.8296	0.6535	0.7938	0.8926	0.8486	0.8763	0.8434	0.7522	0.8903	0.8963	0.8911	0.8815
Average	1	0.7576	0.7252	0.7815	<b>0.8578</b>	0.8344	0.8495	0.8314	0.7659	0.8568	0.8551	0.8484	0.8404

TABLE IV  
Comparison of LRSD for different methods

Images (1358 x 900)	Ori	FLM	LSCN	NPE	LIME	PIE	FBE	Methods					
								SRIE	RRM	ALSM(T=4)	ALSM(T=5)	ALSM(T=6)	ALSM(T=7)
BabyAtWindow	0.0555	0.0461	0.0507	0.0473	0.0558	0.0382	0.0417	0.0438	0.0338	0.0458	0.0467	0.0476	0.0484
BabyOnGrass	0.0500	0.0455	0.0399	0.0326	0.0471	0.0333	0.0358	0.0356	0.0269	0.0404	0.0423	0.0436	0.0445
ChristmasRider	0.0398	0.0341	0.0231	0.0278	0.0367	0.0238	0.027	0.0255	0.0205	0.0302	0.0330	0.0354	0.0372
FeedingTime	0.0342	0.1984	0.2209	0.1637	0.1616	0.1831	0.1531	0.1657	0.1490	0.1772	0.1702	0.1964	0.1593
HighChair	0.1543	0.0291	0.0302	0.1780	0.1815	0.2044	0.1690	0.1825	0.0225	0.0321	0.0336	0.0349	0.0358
LadyEating	0.0288	0.0295	0.0308	0.0439	0.0496	0.0277	0.0305	0.0313	0.0225	0.0351	0.0385	0.0418	0.0430
PianoMan	0.0531	0.0461	0.0377	0.0393	0.0546	0.0328	0.0388	0.0358	0.0337	0.0427	0.0463	0.0494	0.0518
SantasLittleHelper	0.0455	0.0433	0.0307	0.0354	0.0493	0.0294	0.0349	0.0315	0.0234	0.0340	0.0437	0.0479	0.0513
Average	0.0578	0.0590	0.0580	0.071	0.080	0.072	0.066	0.069	<b>0.0415</b>	0.0547	0.0568	0.0621	0.0589

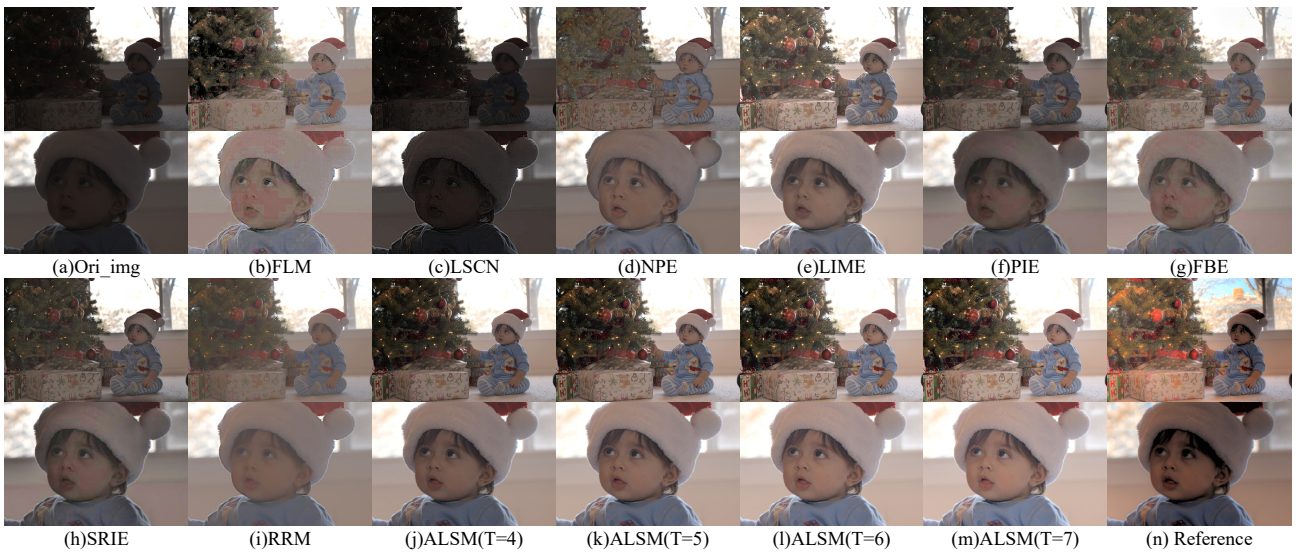


Fig.11. Comparison of enhancement performance for Santa's Little Helper.

#### E. Comparison of computational efficiency

The operation of the ALSM algorithm mainly consists of minimal channel calculation, superpixel segmentation, and MSD calculation in the superpixel. For images with size 1358 x 900 in the HDR dataset, the FLM, LSCN, NPE, LIME, PIE, FBE, SRIE, RRM methods and the proposed ALSM algorithm require approximately 5.61, 16.43, 45.4, 1.26, 5.29, 1.97, 58.31, 80.64 and 282.91 seconds, respectively. Our ALSM exhibits the slowest execution efficiency. In addition, we found that parameter n has little effect on enhancement, and setting T to 6 (or 5) is sufficient for generating satisfying results.

#### IV. CONCLUSION

In this paper, we proposed an effective absorbed light scattering model to explain the absorbed light imaging process

of low-light images, and the absorbed light scattering image generated under sufficient and uniform illumination can effectively reveal hidden details in low-light images. We can achieve the goal of enhancement by regulating atmospheric light and transmittance using this method. Compared with other state-of-the-art methods, the experimental results revealed that our ALSM algorithm achieved a good balance in terms of structure, detail and local feature similarity and exhibited a certain ability to suppress low-density noise. In addition, the full-reference LRSD proposed in this paper is basically consistent with subjective feelings, and this method better reflects the real enhancement effect than the other algorithms. Our enhancement technique is not efficient and does not fundamentally solve the noise amplification problem, and these shortcomings will be addressed in future research.

## REFERENCES

- [1] R. C. Gonzalez, R. E. Woods, and S.L. Eddins, Digital Image Processing. Upper Saddle River, NJ, USA: Prentice-Hall, 2004.
- [2] S. Richard, Computer Vision: Algorithms and Applications. New York, USA: Springer, 2011.
- [3] A. Date, P. V. Ingole, "Low light video enhancement: A Survey," *International Journal of Computer Applications (IJCA)*, vol. 11, no. 2, pp. 4–6, June. 2015.
- [4] J. Yang, X. Jiang, C. Pan, and C.L. Liu, "Enhancement of low light level images with coupled dictionary learning," in Proc. IEEE 23rd Int. Conf. Pattern Recognition, Dec. 2016, pp. 751-756.
- [5] H. Zhao, O. Gallo, I. Frosio, and J. Kautz. Loss functions for image restoration with neural networks. *IEEE Transactions on Computational Imaging*, 3(1), 2017.7
- [6] K. Zhang, W. Zuo, Y. Chen, D. Meng, and L. Zhang. Beyond a Gaussian denoiser: Residual learning of deep CNN for image denoising. *IEEE Transactions on Image Processing*, 26(7), 2017.
- [7] Y. Chen and T. Pock. Trainable nonlinear reaction diffusion: A flexible framework for fast and effective image restoration. *IEEE Transactions on Pattern Analysis and Machine Intelligence*, 39(6), 2017.
- [8] B.L.Cai, X.M.Xu, K.Jia, "DehazeNet: An end-to-end system for single image haze removal," *Transactions on Image Processing(TIP)*, vol.25, no. 11, pp. 5187-5198.2016
- [9] C. Chen, Q. F. Chen, J. Xu, X. Zhang, and V. Koltun, "Learning to see in the dark," in *International conference on Computer Vision and Pattern Recognition (CVPR)*, PP.2782-2790, 2018.
- [10]K. G. Lore, A. Akintayo, and S. Sarkar. LLNet: A deep autoencoder approach to natural low- light image enhancement. *Pattern Recognition*, vol. 61, pp. 650-662, Jan. 2017
- [11]K. Zhan, J. Teng, J. Shi, et al. "Feature-linking model for image enhancement," *Jornal of Electronic Imaging*, vol. 25, no. 6, pp. 2290-2297, 2016.
- [12]K. Zhan, J. Shi, J. Teng, et al. "Linking synaptic computation for image enhancement," *Neurocomputing*, vol. 23, no. 8, pp. 1-12, 2017.
- [13]D. Jobson, Z. Rahman, and G. Woodell, "Properties and performance of a center/surround Retinex," *Transactions on Image Processing (TIP)*, vol. 6, no. 3, pp. 451-462, 1996.
- [14]D. Jobson, Z. Rahman, and G. Woodell, "A multi-scale Retinex for bridging the gap between color images and the human observation of scenes," *Transactions on Image Processing (TIP)*, vol. 6, no. 7, pp. 965-976, 1997.
- [15]X. Fu, D. Zeng, Y. Huang, Y. Liao, X. Ding, and J. Paisley, "A fusion-based enhancing method for weakly illuminated images," *Signal Processing*, vol. 129, pp. 82-96, 2016.
- [16]S. Wang, J. Zheng, H. Hu, and B. Li, "Naturalness preserved enhancement algorithm for non-uniform illumination images," *Transactions on Image Processing (TIP)*, vol. 22, no. 9, pp. 3538-3578, 2013.
- [17]X. Fu, D. Zeng, Y. Huang, X. Zhang, and X. Ding, "A weighted variational model for simultaneous reflectance and illumination estimation," in *International conference on Computer Vision and Pattern Recognition (CVPR)*, PP.2782-2790, 2016.
- [18]X. J. Guo, Y. Li, H. B. Ling, "LIME: Low-light image enhancement via illumination map estimation," *Transactions on Image Processing (TIP)*, vol. 26, no. 2, pp. 982-993, 2017.
- [19]X. Y Fu, Y.H Liao, D.L. Zeng, etc.al, "A probabilistic method for image enhancement with simultaneous illumination and reflectance estimation," *Transactions on Image Processing (TIP)*, vol. 24, no. 12, pp. 4965-4977, 2015.
- [20]M. Li, J. Y. Liu, "Structure-Revealing Low-Light Image Enhancement Via Robust Retinex Model," *Transactions on Image Processing (TIP)*, vol. 27, no. 6, pp. 2628-2841, 2018.
- [21]X. Dong, G.Wang, Y.Pang, W.Li, J. Wen, W. Meng, and Y. Lu, "Fast efficient algorithm for enhancement of low lighting video," in *International Conference on Multimedia and Expo(ICME)*, pp. 1-6, 2011.
- [22]L. K. Choi, J. You, A. C. Bovik, "Referenceless prediction of perceptual fog density and perceptual image defogging," *Transactions on Image Processing (TIP)*, vol. 24, no. 11, pp. 3888-3901, 2015.
- [23]X. X. Pan, F. Xie, Z. G. Jiang, "Haze removal for a single remote sensing image based on deformed haze imaging model," *Signal Processing Letters*, vol. 22, no. 10, pp. 1806-1810, 2015.
- [24]R. Fattal, "Dehazing using color- lines," *ACM Transactions on graphics*, vol. 28, no. 4, pp. 1-11, 2013.
- [25]Z. G. Li, J. H. Zheng, "Edge-preseving decomposition-based single image haze removal," *Transactions on Image Processing (TIP)*, vol. 24, no. 12, pp. 5432-5441, 2015.
- [26]C. O. Ancuti, C. Ancuti, "Single image dehazing by multi-scale fusion," *Transactions on Image Processing (TIP)*, vol. 22, no. 8, pp. 3271-3282, 2013.
- [27]R. Fattal, "Single image dehazing," *ACM Transactions on graphics*, vol. 27, no. 3, pp. 1-9, 2008.
- [28]J. P. Tarel, N. Hautiere, "Fast visibility from a single color or gray level image," in *Computer Vision*, pp. 2201-2208, 2009.
- [29]K. M. He, J. Sun, X. X. Tang, "Single image haze removal using dark channel prior," *Transactions on Pattern Analysis and Intelligence (PAMI)*, vol. 33, no. 12, pp. 2341-2353, 2011.
- [30]K. M. He, "Single image haze removal using dark channel prior," Ph.D. dissertation, Information Engineering, Hong Kong Univ., Hong kong., China, 2011.
- [31]A.Galdran. "Image dehazing by artificial multiple-exposure image fusion," *Signal Processing*, vol.149, pp. 135-147.2018.
- [32]L.K. Choi, J. You, A.C. Bovik, "Referenceless prediction of perceptual fog density and perceptual image defogging," *Transactions on Image Processing (TIP)*, vol.24, no. 11, pp. 3888-3901.2015.
- [33]Y. H. Shiau, P. Y. Chen, H. Y. Yang, C. H. Chen, S. S. Wang, "Weighted haze removal method with halo prevention," *Journal of Visual Communication and Image Representation (VCIR)*, vol. 25, no. 3, pp. 445-453, 2014.
- [34]Y. L. Tian, C. Xiao, X. Chen, D. Q. Yang, "Haze removal of single remote sensing image by combining dark channel prior with super-pixel," *Visual Information and Communication*, PP. 1-6, 2016.
- [35]K.B. Gibson, D.T. Vo, T.Q. Nguyen, "An investigation of dehazing effects on image and video coding," *Transactions on Image Processing (TIP)*.vol. 21, no. 2, pp. 662-673, 2012.
- [36]S. G. Narasimhan, S. K. Nayar, "Chromatic Framework for Vision in Bad Weather," *Computer Vision and Pattern Recognition (CVPR)*, vol. 1, pp. 598-605, June 2000.
- [37]S. G. Narasimhan, S. K. Nayar, "Vision and the Atmosphere," *Int'l J. Computer Vision*, vol.48, pp. 233-254, June 2002.
- [38]A. Levinstein, A. Stere, K. Kutulakos, et al, "Turbopixels: fast superpixels using geometric flows," *Transactions on Pattern Analysis and Intelligence (PAMI)*, vol. 31, no. 12, pp. 2290-2297, 2009.
- [39]S. Zhu, D. H. Cao, S. X. Jiang, et al. "Fast super-pixel segmentation by iterative edge refinement," *International Electronics Letters*, vol. 51, no. 3, pp. 230-232, 2015.
- [40]J. B. Shi, Y. F. Du, W. G. Wang, "Lazy random walks for super-pixel segmentation," *Transactions on Image Processing(TIP)*, vol. 23, no. 4, pp. 1451-1462, 2014.
- [41]R. Achanta, A. Shaji, K. Smith, "SLIC super-pixels compared to state-of-the-art super-pixel methods," *Transactions on Pattern Analysis and Intelligence (PAMI)*, vol. 34, no. 11, pp. 2274-2282, 2012.
- [42]P. Neubert, P. Protzel, "Super-pixel benchmark and comparison," Proc. of forum bildverarbeitung, regensburg, Germany, 2012.
- [43]NASA. (2001). Retinex Image Processing. [Online]. Available: <http://dragon.larc.nasa.gov/retinex/pao/news>.
- [44]K. M. He, J. Sun, X. X. Tang, "Guided image filtering," *Transactions on Pattern Analysis and Intelligence (PAMI)*, vol. 35, no. 11, pp. 1-13, 2013.
- [45]K. Matkovic, L. Neumann, A. Neumann, T. Psik, "Global contrast factor- a new approach to image contrast", in *Computational Aesthetics in Graphics, Visualization and Imaging*, pp. 159-168, 2005.
- [46]K. Gu, W. Lin, G. Zhai, X. Yang, and C. W. Chen, "No-reference quality metric of contrast-distorted images based on information maximization," *IEEE Trans. Cybern*, vol. 47, no. 12, pp. 4559-4565, Dec.2017.
- [47]K. Gu, D. C. Tao, J. F. Qiao, W. S. Lin, "Learning a no-reference quality assessment model of enhanced images with big data," *Transactions on Neural Networks and Learning Systems*, vol. 29, no. 4, pp. 1301-1313.
- [48]P. Sen, N. Kalantari, M. Yaesoubi, S. Darabi, D. Goldman, and E. Shechtman, "Robust patch-based hdr reconstruction of dynamic scenes," *TOG*, vol. 31, no. 6, pp.203:1=203:11,2012.
- [49]Z. Wang, Q. Li, "Information content weighting for perceptual image quality assessment," *Transactions on Image Processing (TIP)*, vol. 20, no. 5, pp. 1185-1198, 2011.